

Thermal stability of CrN_x nanometric coatings deposited on stainless steel

Carlo Paternoster · Alberto Fabrizi ·
Raimondo Cecchini · Mohamad El Mehtedi ·
Patrick Choquet

Received: 6 July 2007 / Accepted: 7 December 2007 / Published online: 6 March 2008
© Springer Science+Business Media, LLC 2008

Abstract Thin CrN_x coatings are often used as protective coatings for steel. In these applications, coated parts might be subjected to high temperatures that can alter the coatings structural and mechanical properties. In this work, the properties of nanometric CrN_x coatings deposited by reactive magnetron sputtering on AISI 304L stainless steel were studied by transmission electron microscopy, glazing incident X-ray diffraction, Atomic Force Microscopy, and nanoindentation. The effect of annealing, both in air and vacuum, on the coating crystal structure, surface morphology and hardness were also investigated. It was found that annealing in vacuum-induced phase transformation from CrN to Cr₂N, while after annealing in air only Cr₂O₃ phase was present. Surface roughness did not increase for annealing in vacuum. CrN_x coatings with higher Cr₂N phase content showed lower roughness increase for annealing in air. Measured hardness was >10 GPa for as-deposited CrN_x samples. An increase in hardness up to >20 GPa was found for vacuum-annealed samples.

Introduction

Among protective coatings, CrN_x represents one of the most commonly studied and employed materials. Besides of good resistance to wear and corrosion and low friction

coefficient, it has high hardness and good thermal barrier properties [1–4].

In many industrial applications (e.g., automotive, construction, decorative), CrN_x is used as protective coating for steel [5]. In such cases, the coating deposition is often required on large parts and components and must guarantee high throughput. Physical vapor deposition is able to produce high-quality coatings and allows for a precise control of deposition parameters, such as the applied bias and the gas flow rates in the reactive atmosphere, which are responsible for the film structural, morphological, and mechanical properties [6–9]. The samples studied in this work were deposited by Cockerill Sambre ARCELORMITTAL S. A. (Belgium) steel company, using a specifically designed reactive magnetron sputtering apparatus for in-line coating of flat stainless steel coils of 1.5 m width. This apparatus allows for continuous production, with speed line of 5–15 m/min.

In their applications, CrN_x coated parts are often exposed to high temperature. This can cause phase transformation, oxidation, and the change of the mechanical properties in the coating [10, 11]. Due to their unique mechanical properties, special interest is growing around very thin and nano-structured coatings [12, 13]. However, few studies have been dedicated to thermal stability of very thin protective coatings, such as CrN_x, on steel.

In this work, the behavior of 110–210 nm thick CrN_x coatings, deposited by reactive magnetron sputtering on AISI 304L stainless steel and subjected to thermal annealing both in air and vacuum, was investigated. Transmission electron microscopy (TEM) and glazing incident X-ray diffraction (GIXRD) were used to study crystal structure, atomic force microscopy (AFM) for surface morphology evolution and nanoindentation for measuring hardness.

C. Paternoster (✉) · A. Fabrizi · R. Cecchini · M. El Mehtedi
Department of Mechanics, Università Politecnica delle Marche,
via Brecce Bianche, 60131 Ancona, Italy
e-mail: c.paternoster@univpm.it

P. Choquet
ARCELOR Research Liège, Bld de Colonster B57,
B4000 Liège, Belgium

Experimental

Three CrN_x coated AISI 304L stainless steel (composition in mass %: 10% Ni, 18% Cr, bal. Fe) samples types, in the following indicated by A, B, and C, were fabricated by ARCELOR. Flat AISI 304L sheets of 1.5 m with and thickness of 0.6 mm were pre-treated by Ar-plasma etching and coated using direct current reactive sputtering in an Ar/N₂ mixture atmosphere. Plasma composition was monitored by optical emission spectroscopy during deposition. Deposition conditions were defined by the Cr/Ar ionic ratios in the plasma and N₂ flow. Cr/Ar ratios were: 0.65, 0.65, and 0.85 for sample A, B, and C, respectively. Three different N₂ flow regimes were used: high for sample A, medium for sample B, and low for sample C.

From each type of the coated sheets, several samples of 1 cm × 2 cm were extracted and cut using a water-cooled precision diamond blade. Coatings thicknesses were measured by AFM on the samples, resulting (210 ± 10), (140 ± 10), and (110 ± 10) nm for samples A, B, and C, respectively. Samples characteristics are summarized in Table 1.

The microstructure of the deposited coatings was characterized by a PHILIPS[®] CM200 TEM in plane view at 200 keV. GIXRD measurements were recorded by an INEL[®] CPS120 diffractometer operated at 40 kV and 30 mA, with Cu K α radiation ($\lambda_{\text{Cu K}\alpha} = 0.154$ nm). Surface morphology and surface roughness were investigated by a BURLEIGH INSTRUMENTS[®] Metris-2001 AFM operated in contact mode. The coatings' hardness was measured using a HISITRON[®] Ubi HT Nanoindenter with a Berkovich diamond tip. The tip calibration was performed using reference-fused quartz. Unload curve analysis was done according to the Oliver and Pharr method [14].

Thermal annealing was performed at 650 °C both in air and vacuum ($2.0 \cdot 10^{-4}$ Pa) for 1, 2, 4, and 8 h. After annealing, samples were left to cool in air and vacuum at room temperature.

Results and discussion

Microstructure investigation

Figure 1 shows TEM bright field images of sample A in plane view at different magnifications. At low magnification (Fig. 1a), the substrate grain boundaries and the slip bands formed in the rolling stage of the steel are visible [15]. At higher magnification (Fig. 1b), the CrN_x crystal structure is visible, showing a very fine structure, with grain sizes ranging from 15 to 35 nm. CrN_x grains seem to be elongated in one direction. Similar observations were reported for CrN_x sputtered on Silicon in another work

Table 1 Summary of samples A, B, and C characteristics: deposition conditions (Cr/Ar ratio and N₂ flow) and thickness measured by AFM. sccm, standard cubic centimeters per minute

Samples	Plasma Cr/Ar ionic ratio	N ₂ flow (sccm)	thickness (nm)
A	0.65	120	210 ± 10
B	0.65	90	140 ± 10
C	0.85	60	110 ± 10

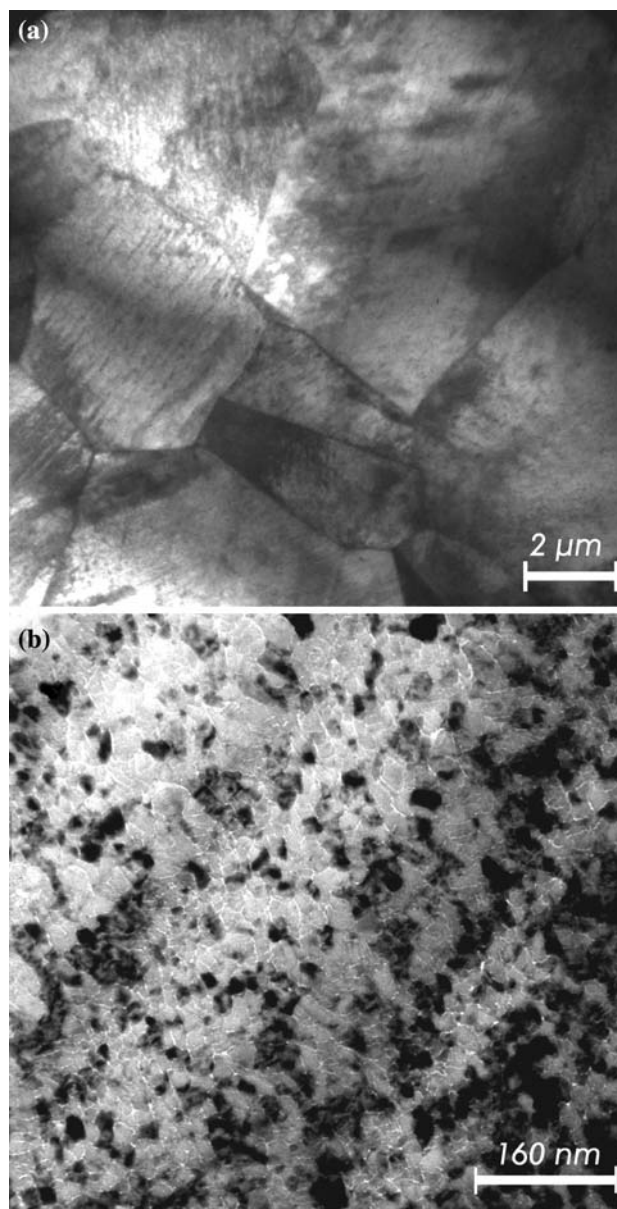


Fig. 1 TEM in plane view of sample A showing: (a) substrate grain boundaries and the slip bands at low magnification (2,000 \times), and (b) CrN_x coating microstructure at higher magnification (38,000 \times)

[16], and elongation of the grains was explained with the geometrical orientation of the sample substrate with respect to the target during sputtering. No detectable presence of

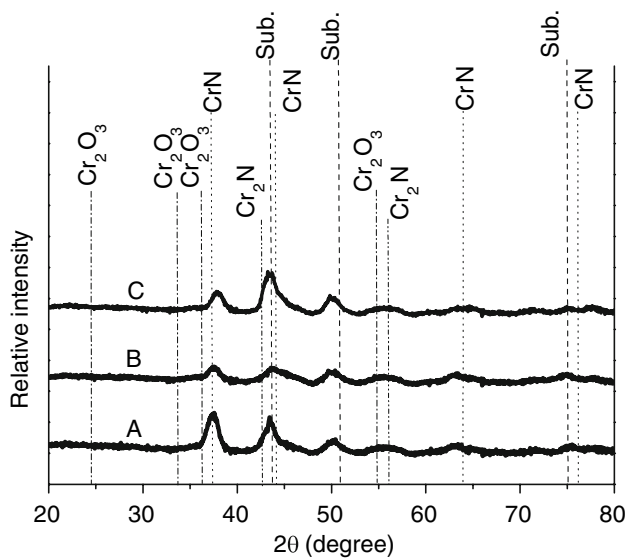


Fig. 2 GIXRD patterns of samples A, B, and C in as-deposited conditions

incorporated Argon was found on the samples by energy dispersive X-ray spectroscopy system of TEM.

Figure 2 shows the GIXRD measurements performed on the as-deposited Cr_xN /steel samples. The peaks at angles of 43.6° , 50.8° , and 74.8° are due to substrate (111), (200), and (220) planes of austenitic steel, respectively. The peak at angle 37.4° is instead due to the CrN (111) plane. A contribution from CrN (200) on the peak at 43.6° is also possible. The intensity of the CrN peaks relative to the substrate peaks intensity decreases from samples A to C, indicating some difference in the phase of the samples. Both CrN and Cr_2N phases have been reported in reactively sputtered CrN_x films, depending on the Ar to N_2 flow ratio during deposition [16]. CrN (111) or (200) and Cr_2N (002) or (111) textures were reported for as-deposited CrN_x films sputtered on silicon (100) substrates, depending on the details of the deposition [8]. In particular the fraction of Cr_2N versus CrN is found to increase as N_2/Ar flow rate ratio is decreased, with the presence of both phases for very low N_2/Ar flow ratios [2, 4, 8, 17]. Although no clear evidence of Cr_2N phase is present the as-deposited samples, a contribution on the peak at 43.6° from Cr_2N (111) plane is possible. The relative reduction of CrN peaks and increase in contribution from Cr_2N (111) peak measured in all the samples (Fig. 1) is consistent with the progressive reduction of N_2 flow during sputtering. No presence of chromium oxide phase is visible on the as-deposited samples.

In Fig. 3 are reported the GIXRD diffraction patterns for all the samples, after thermal annealing in vacuum at 650°C for increasing annealing times. Also the diffraction pattern

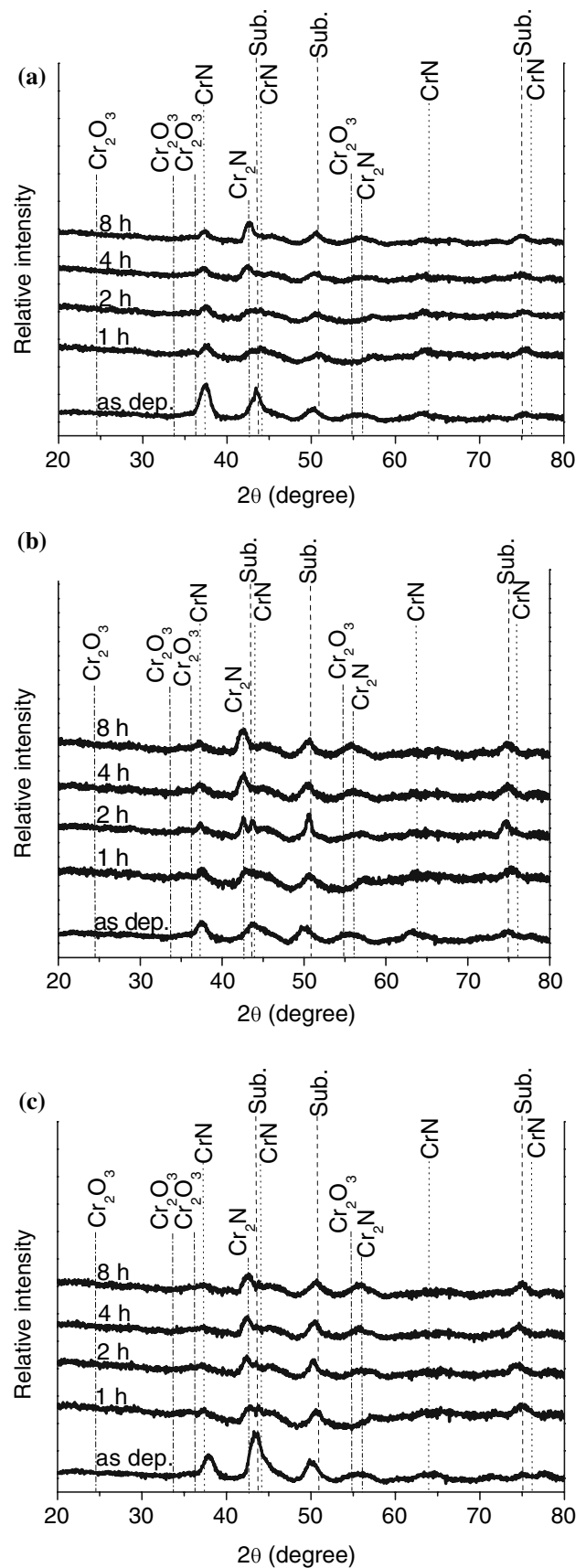


Fig. 3 GIXRD patterns of: (a) sample A, (b) sample B, and (c) sample C after annealing at 650°C in air for 1, 2, 4, and 8 h

of the as-deposited samples is reported. The intensity of all the peaks recorded on the as-deposited samples is much decreased on the annealed samples. From Fig. 3 it can be seen that the annealed samples show a clear peak at 42.6° , consistent with diffraction from Cr_2N (111) planes. The evolution of samples A and C diffraction patterns with respect to Cr_2N (111) peak presents the most relevant differences. For sample A, the intensity of Cr_2N (111) peak relative to CrN (111) and substrate peaks increases progressively with annealing time; for sample C, the diffraction pattern changes with annealing time are very small. Phase transformation of CrN_x films upon thermal anneal in air, vacuum, and controlled atmosphere was investigated by other authors [8, 17–22]. In some of these works, phase transformation from CrN to Cr_2N , upon thermal annealing in vacuum, has been observed [19, 21]. In some other works, Cr_2N phase formation was observed under conditions for which it cannot be explained by thermodynamic considerations [20]. It has been pointed out that phase transformation from CrN to Cr_2N phase can involve both thermodynamic and non-thermodynamic factors, such as stress relaxation-induced phase transformation [18].

The Cr_2N phase in the sample C coating is present for all the treatment conditions, and no relevant changes in the intensity of the related peaks are reported. This phase is not subjected to a further structure evolution for the investigated annealing times, while samples A and B CrN coatings are subjected to a clear phase change, due to different and sometimes opposite factors (Fig. 2). The presence of Cr_2N in sample C is consistent with the lower N_2 flow used for sample C, compared to samples A and B. The evolution of sample B diffraction pattern with annealing in vacuum is intermediate between samples A and C. The diffraction patterns reported in Fig. 3 also confirm that, as expected, no chromium oxidation is occurring during vacuum annealing.

The diffraction patterns of samples A and C after annealing at 650°C in air are reported in Fig. 4. As it can be seen, peaks corresponding to the Cr_2O_3 phase appear on the diffraction patterns from 1 h annealing, with intensity increasing with annealing time. At the same time, CrN phase peaks intensity decreases and have almost completely disappeared for 8 h annealing, when only substrate and chromium oxide peaks are still present on the diffraction patterns. Samples A and C show a similar diffraction patterns evolution upon annealing in air, as illustrated in Fig. 4. Though, sample C shows Cr_2O_3 peaks with higher intensity than sample A for 4 and 8 h annealing times, especially for the peaks at 33.6 and 54.9° corresponding to (104) and (116) Cr_2O_3 planes. As for annealing in vacuum, also for annealing in air sample B, shows an intermediate behavior between samples A and C.

Chromium oxidation in CrN_x films after thermal annealing in air was described by several other authors [17,

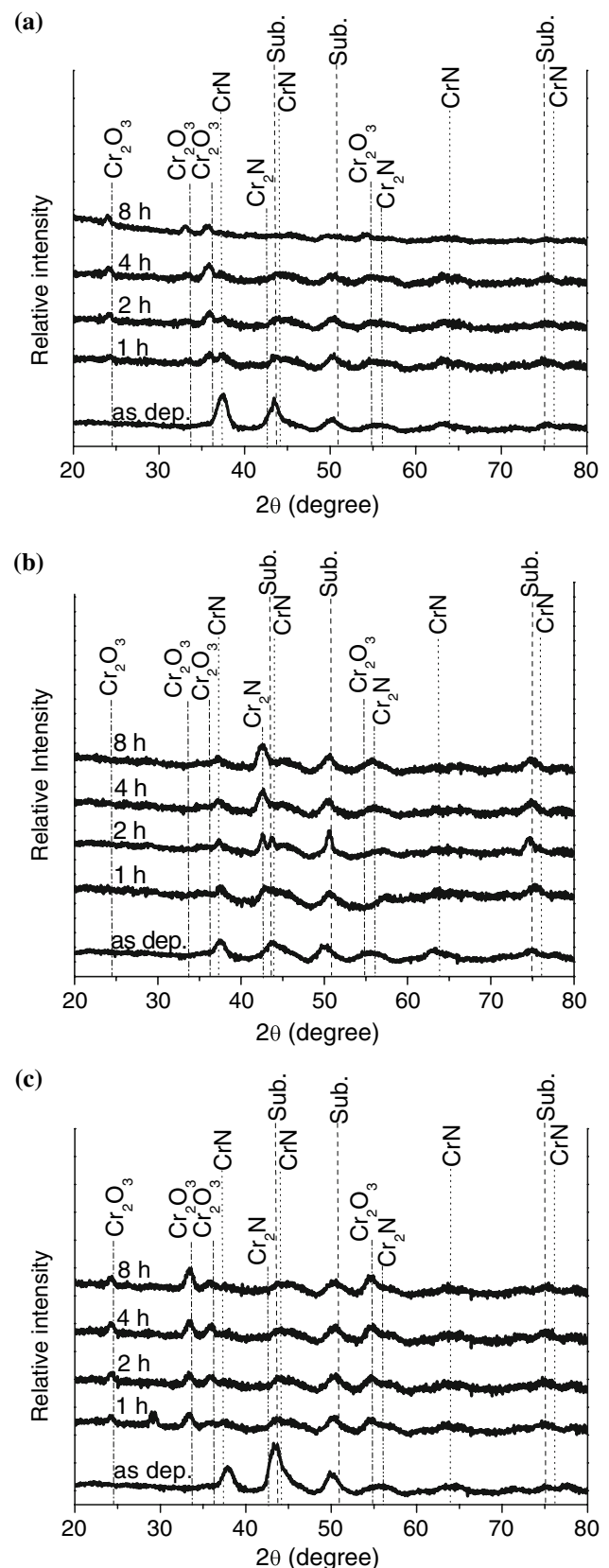


Fig. 4 GIXRD patterns of: (a) sample A, (b) sample B, and (c) sample C after annealing at 650°C in vacuum for 1, 2, 4, and 8 h

23–26] and can be explained on the basis of thermodynamic considerations. The change in the Gibbs free energy associated with the oxidation reactions of, respectively, CrN and Cr₂N can be written as follows:

$$2\text{CrN}_{(s)} + \frac{3}{2}\text{O}_{2(g)} = \text{Cr}_2\text{O}_{3(s)} + \text{N}_{2(g)}$$

$$\Delta G = \Delta G^0 + RT \ln \left(\frac{p_{\text{N}_2}}{p_{\text{O}_2}^{3/2}} \right)$$

$$= (-883.368 + 0.101 \times T) + RT \ln \left(\frac{p_{\text{N}_2}}{p_{\text{O}_2}^{3/2}} \right) \text{ (kJ/mol)}$$

(1)

$$\text{Cr}_2\text{N}_{(s)} + \frac{3}{2}\text{O}_{2(g)} = \text{Cr}_2\text{O}_{3(s)} + \frac{1}{2}\text{N}_{2(g)}$$

$$\Delta G = \Delta G^0 + RT \ln \left(\frac{p_{\text{N}_2}^{1/2}}{p_{\text{O}_2}^{3/2}} \right)$$

$$= (-1010.937 + 0.200 \times T) + RT \ln \left(\frac{p_{\text{N}_2}^{1/2}}{p_{\text{O}_2}^{3/2}} \right) \text{ (kJ/mol)}$$

(2)

where ΔG represents the change in the Gibbs free energy for this transformation; ΔG^0 is the standard Gibbs free energy; R is the gas constant; T [K] is the absolute temperature; p_{N_2} is the partial pressure of nitrogen and p_{O_2} is the partial pressure of oxygen [20]. Using Eqs. 1 and 2 to calculate Gibbs free energy change of both reactions for the present conditions ($T = 650 \text{ }^\circ\text{C} = 932.16 \text{ K}$, air: $p_{\text{N}_2} = 0.79 \text{ atm}$ and $p_{\text{O}_2} = 0.21 \text{ atm}$) gives, respectively, ΔG equal to -774 and -809 kJ/mol for CrN and Cr₂N, respectively. This implies that in the present case both phases tend to oxidize to Cr₂O₃ under present conditions.

Furthermore, Cr₂N oxidation is expected to be sped up having a lower activation barrier: in the discussed case, in which the ratio $p_{\text{N}_2}^{1/2}/p_{\text{O}_2}^{3/2}$ is constant and equal to ~ 9 , the driving force depends on the temperature and it is larger for the oxidation of Cr₂N than for the oxidation of CrN, as evident from the values obtained. For the process atmosphere above considered, the oxidation of CrN is generally easier for temperatures higher than $1,010 \text{ }^\circ\text{C}$, while the oxidation of Cr₂N would be easier for lower temperatures.

As discussed above, sample C is expected to have a higher Cr₂N content. This can explain the higher intensity of Cr₂O₃ peaks for a given annealing time on sample C compared to sample A (Fig. 1).

Surface morphology

The surface morphologies properties of the as-deposited and annealed samples were studied by AFM. Images of $4 \times 4 \text{ }\mu\text{m}^2$ scan size areas were used to calculate the root

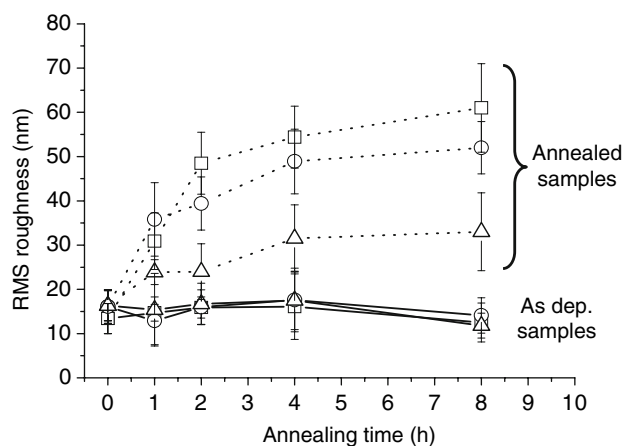


Fig. 5 Root mean square (RMS) surface roughness of as-deposited samples and after thermal annealing at $650 \text{ }^\circ\text{C}$ for 1, 2, 4, and 8 h in air: sample A ($\dots\Box\dots$), sample B ($\dots\circ\dots$), and sample C ($\dots\Delta\dots$); and vacuum: sample A ($-\Box-$), sample B ($-\circ-$), and sample C ($-\Delta-$)

mean square (RMS) surface roughness of the as-deposited and thermally annealed samples, which are reported in Fig. 5. Surface morphology evolution of sample B upon annealing at $650 \text{ }^\circ\text{C}$ for 1, 2, 4, and 8 h in air and in vacuum is shown in Figs. 6 and 7, respectively, where 3-dimensional AFM images of $2 \times 2 \text{ }\mu\text{m}^2$ scan size areas are reported.

Samples A, B, and C show RMS surface roughness values fairly comparable, and close to 15 nm (Fig. 5), in the as-deposited condition. Annealing in air leads to a significant increase in surface roughness, starting from 1 h annealing time. As it is shown by Fig. 6, surface morphology of the coating changes and larger features appear on the coating topography. These are most likely to be Cr₂O₃ crystallites, resulting from the oxidation of the CrN_x coatings, as indicated by the GIXRD analyses. From Fig. 5 it can be seen that the RMS surface roughness values of sample C after the thermal annealing in air are smaller than those of samples A and B, for all the annealing times. This can be explained by the formation of smaller oxide crystallites on sample C compared to samples A and B. The oxide crystallite size increase up to 2 h of annealing time for all the samples and for longer times the crystallites vary in size from approximately 250–350 nm and from 150 to 250 nm, respectively, for the samples A, B, and C. Similar morphological evolution produced by chromium oxidation has been largely reported in the literature [24–27]. Thermal annealing in vacuum does not affect the RMS surface roughness values and morphology of samples A, B, and C for the all the annealing times, as it can be seen from Figs. 5 and 7.

Mechanical properties

Nanoindentation has been used to calculate hardness using indentation load–displacement data. Figure 8 shows the

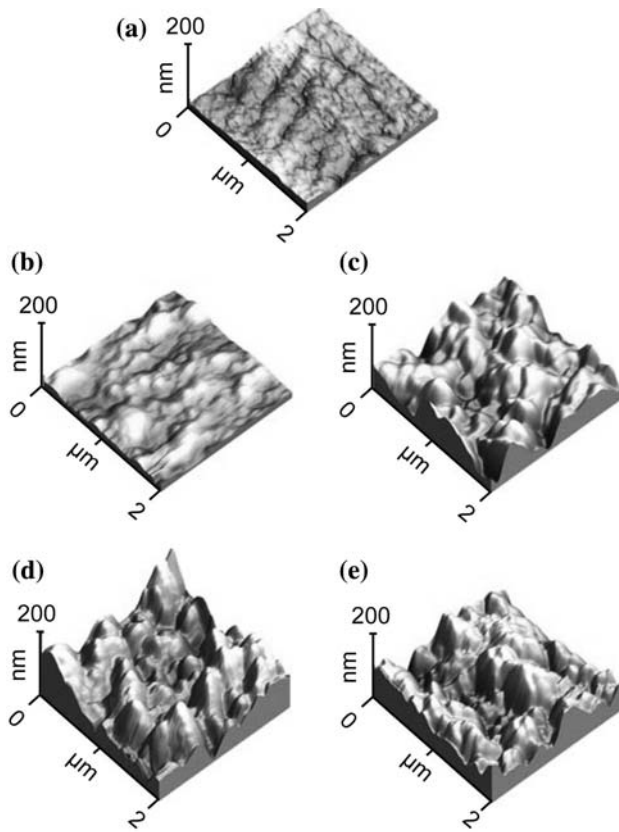


Fig. 6 AFM surface morphology of (a) as-deposited sample B and after annealing at 650 °C in air for: (b) 1 h, (c) 2 h, (d) 4 h, and (e) 8 h

hardness of samples A, B, and C as-deposited and after 8 h of annealing in vacuum as a function of penetration depth.

From Fig. 8, it is seen that hardness decreases with penetration depth for all the as-deposited and vacuum-annealed samples. This behavior is typically observed as of the influence of the substrate on the measured hardness [28–30]. A ‘rule of thumb’ requires that penetration depth is kept below 1/10 of the film thickness to contain the deformation within the film. On the other hand, relatively high penetration depths are required to achieve measurements not affected by the roughness of the system. Furthermore, for penetration depths near or lower than the indenter tip radius, the area function calibration is not reliable. For very thin films, these conditions are difficult to achieve, and measured hardness is often affected by the substrate [31, 32]. For AFM investigations showed that as-deposited and vacuum-annealed samples have an RMS surface roughness around 15 nm, which requires indentation depths above this value. As film thicknesses involved in the present work are in the range of 100–200 nm, for these penetration depths the influence of the substrate on the measured hardness is expected.

Hardness of samples A, B, and C was measured for penetration depths starting from 15 nm. Largest

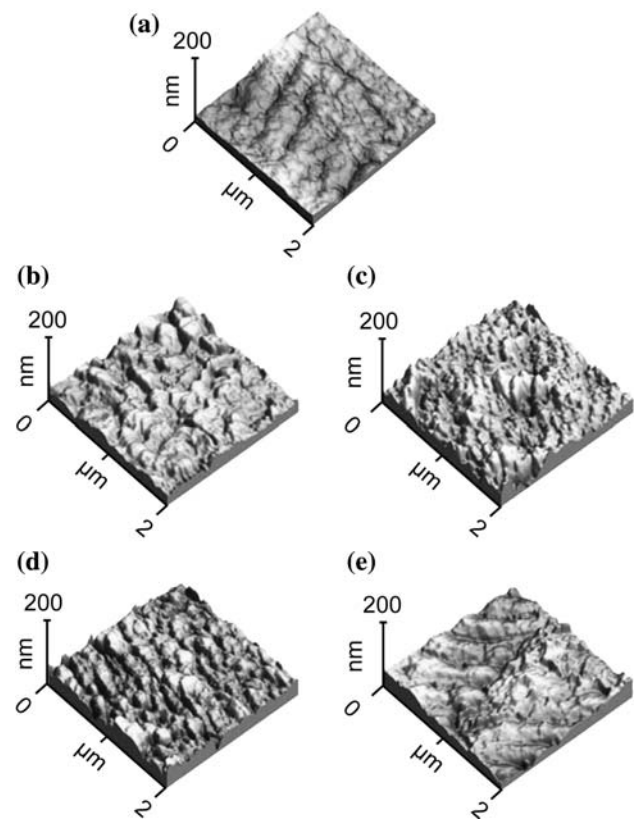


Fig. 7 AFM surface morphology of (a) as-deposited sample B and after annealing at 650 °C in vacuum for: (b) 1 h, (c) 2 h, (d) 4 h, and (e) 8 h

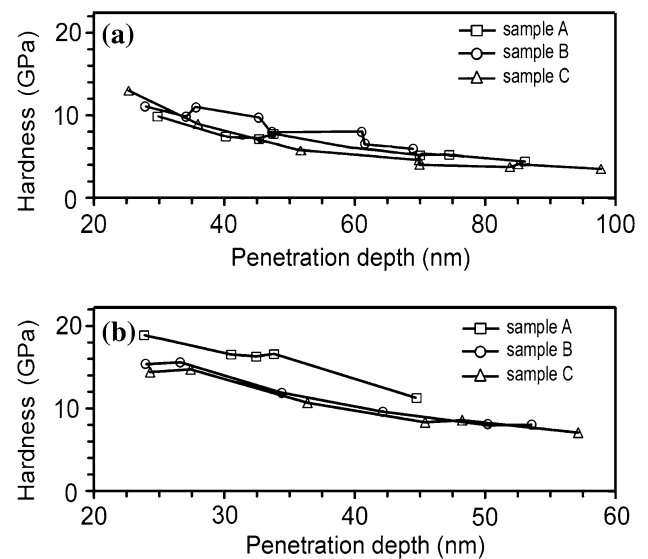


Fig. 8 Hardness evaluation through nanoindentation. (a) As-deposited samples and (b) after annealing in vacuum at 650 °C for 8 h of: sample A (—□—), sample B (—○—), and sample C (—△—)

penetration depths were kept below the film thickness. The hardness behavior as a function of penetration depth is typical of that of a film with higher hardness than the

substrate: for small penetration depth, the measured hardness approaches the hardness of the film, whereas for high penetration depths the measured hardness approaches that of the substrate. For all samples, the measured hardness tends to about 4.5 GPa for large penetration depths. This value is consistent with the hardness measured on uncoated regions of substrate and are close to the value reported for AISI 304L [33]. For the smallest penetration depths that can be considered not affected by roughness and tip calibration, i.e., 30 nm, the hardness of as-deposited CrN_x approaches values of about 10 GPa (Fig. 8a). The true hardness of the as-deposited film should then be >10 GPa. A noticeable increase in hardness for all the samples is found after annealing in vacuum (Fig. 8b), with higher increase in sample A. Due the large increase in roughness after annealing in air (Fig. 5), it was not possible to obtain reliable nano-hardness measurements for these sample conditions.

Changes of hardness in CrN_x coatings after annealing in vacuum have been reported in other works [8, 34]. As for measurements on the as-deposited samples, the measured hardness depends on the penetration depth, and it can be concluded that the true hardness is >20 GPa for sample A, and >15 GPa for samples B and C. Nano-hardness of sputtered CrN_x films has been studied only for thicknesses greater than ~500 nm whereas no other work has been reported for thickness in the range considered in the present one. The reported values of CrN_x hardness are quite scattered [8, 31, 34–36] and in the range of 10–30 GPa. The change in hardness upon anneal can be attributed to two different factors: microstructure and phase transformations and stress relaxation. The CrN_x films studied in this work, as in other, are expected to have a compressive stress, due to the different thermal expansion coefficients of CrN ($2.3 \cdot 10^{-6} \text{ K}^{-1}$) [23] and AISI 304L ($\sim 17.8 \cdot 10^{-6} \text{ K}^{-1}$) [5]. Relaxation of compressive stress of CrN_x coatings is expected to occur in the temperature range of 400–600 °C [20] and should be accompanied by a reduction of hardness. In the present work, the increase in hardness indicates that changes in microstructure are compensating the negative trend due to stress relaxation. The higher increase in hardness was found in sample A, as CrN to Cr₂N phase transformation was wider, whereas samples C and B, for which hardness change is lower, showed minor microstructure changes (see GIXRD data of Fig. 3.)

Conclusions

Crystal structure, surface morphology, and hardness of thin CrN_x coatings, deposited by reactive sputtering on AISI 304L stainless steel sheets, were investigated after deposition and after thermal annealing in air and vacuum.

Transmission electron microscopy inspections showed that the as-deposited coatings have a very fine grain structure. CrN phase was found on all the samples, with a predominant (111) texture. Annealing in vacuum induced formation of Cr₂N phase with (111) texture from CrN phase. Anneal in air-induced formation of Cr₂O₃ phase, with higher oxidation speed for CrN phase. Surface roughness increased for all the samples after annealing in air and large features appeared on the surface, as a consequence of Cr₂O₃ phase formation. CrN_x coatings with higher Cr₂N phase content showed lower roughness increase. Annealing in vacuum did not modify significantly surface roughness and morphology of the CrN_x coatings for all the samples.

Film hardness was above 10 GPa for as-deposited CrN_x. Annealing in vacuum was found to increase hardness for all the samples, as a consequence of microstructure changes overcoming stress relaxation phenomena.

Acknowledgements The authors are grateful to Prof. S. Spigarelli and Prof. M. Cabibbo for the useful discussions. This research has been funded by EU-EXCELL Project NoE 5157032 (web site: www.no-e-excell.net).

References

- Schramm BC, Scheerer H, Hoche H, Broszeit E, Abele E, Berger C (2004) *Surf Coat Technol* 188–189:623
- Polcar T, Parreira NMG, Novák R (2007) *Surf Coat Technol* 201:5228
- Randhawa H (1988) *Surf Coat Technol* 36:829
- Pradhan SK, Nouveau C, Vasin A, Djouadi MA (2005) *Surf Coat Technol* 200:141
- ASM Specialty Handbook: Stainless Steels (1994) ASM International, Materials Park, OH, USA, pp 1–12
- Feng HP, Hsu CH, Lu JK, Shy YH (2003) *Mater Sci Eng A* 347:123
- Aubert A, Gillet R, Gaucher A, Terrat JP (1983) *Thin Solid Films* 108:165
- Wei G, Rar A, Barnard JA (2001) *Thin Solid Films* 398–399:460
- Barata A, Cunha L, Moura C (2001) *Thin Solid Films* 398–399:501
- Lu FH, Chen HY, Hung CH (2003) *J Vac Sci Technol A* 21(3):671
- Chang KL, Chung SC, Lai SH, Shih HC (2004) *Appl Surf Sci* 236:406
- Gleiter H (2000) *Acta Mater* 48:1
- Komiya S, Ono S, Umezu N (1977) *Thin Solid Films* 45:473
- Oliver WC, Pharr GM (1992) *J Mater Res* 7:1564
- ASM handbook: metallography and microstructure (2004) ASM International, Materials Park, OH, USA, pp 684–691
- Zhao ZB, Rek ZU, Yalisove SM, Bilello JC (2005) *Thin Solid Films* 472:96
- Mayrhofer PH, Tischler G, Mitterer C (2001) *Surf Coat Technol* 142–144:78
- Chen HY, Lu FH (2003) *J Mater Sci Lett* 22:817
- Herr W, Broszeit E (1997) *Surf Coat Technol* 97:335
- Lu FH, Chen HY (2001) *Thin Solid Films* 398–399:368
- Héau C, Fillit RY, Vaux F, Pascaretti F (1999) *Surf Coat Technol* 120–121:200

22. Odén M, Almer J, Håkansson G, Olsson M (2000) *Thin Solid Films* 377–378:407
23. Castaldi L, Kurapov D, Reiter A, Shklover V, Schwaller P, Patscheider J (2007) *Surf Coat Technol.* doi:[10.1016/j.surfcoat.2007.05.070](https://doi.org/10.1016/j.surfcoat.2007.05.070)
24. Mayrhofer PH, Willmann H, Mitterer C (2001) *Surf Coat Technol* 146:222
25. Wang DY, Lin JH, Ho WY (1998) *Thin Solid Films* 332:295
26. Barshilia BHC, Jain A, Rajam KS (2004) *Vacuum* 72:241
27. Chen HY, Lu FH (2006) *Thin Solid Films* 515:2179
28. Tuck JR, Korsunsky AM, Bull SJ, Davidson RI (2001) *Surf Coat Technol* 137:217
29. Puchi-Cabrera ES (2002) *Surf Coat Technol* 160:177
30. Korsunsky AM, McGurk MR, Bull SJ, Page TF (1998) *Surf Coat Technol* 99:171
31. Ichimura H, Ando I (2001) *Surf Coat Technol* 145:88
32. Tu JN, Duh JG, Tsai SY (2000) *Surf Coat Technol* 133–134:181
33. Kostov KG, Ueda M, Lepiensky M, Soares PC Jr, Gomes GF, Silva MM, Reuther H (2004) *Surf Coat Technol* 186:204
34. Herr W, Broszeit E (1997) *Surf Coat Technol* 97:669
35. Cunha L, Andritschky M, Pischow K, Wang Z (1999) *Thin Solid Films* 355–356:465
36. Lee JW, Tien SK, Kuo YC, Chen CM (2006) *Surf Coat Technol* 200:3330